The effect of the dynamic surface bareness on dust source function, emission, and distribution

Dongchul Kim,[1,2,3] Mian Chin,[2] Huisheng Bian,[1,2] Qian Tan,[2,3] Molly E. Brown,[2] Tai Zheng,[4,5] Renjie You,[6,7] Tomas Diehl,[2,3] Paul Ginoux,[8] and Tom Kucsera[2,3]

Received 6 April 2011; revised 18 September 2011; accepted 5 November 2012; published 17 January 2013.

[1] In this study we report the development of a time dependency of global dust source and its impact on dust simulation in the Goddard Chemistry Aerosol Radiation and Transport (GOCART) model. We determine the surface bareness using the 8 km normalized difference vegetation index (NDVI) observed from the advanced very high resolution radiometer satellite. The results are used to analyze the temporal variations of surface bareness in 22 global dust source regions. One half of these regions can be considered permanent dust source regions where NDVI is always less than 0.15, while the other half shows substantial seasonality of NDVI. This NDVI-based surface bareness map is then used, along with the soil and topographic characteristics, to construct a dynamic dust source function for simulating dust emissions with the GOCART model. We divide the 22 dust source regions into three groups of (I) permanent desert, (II) seasonally changing bareness that regulates dust emissions, and (III) seasonally changing bareness that has little effect on dust emission. Compared with the GOCART results with the previously employed static dust source function, the simulation with the new dynamic source function shows significant improvements in category II regions. Even though the global improvement of the aerosol optical depth (AOD) is rather small when compared with satellite and ground-based remote sensing observations, we found a clear and significant effect of the new dust source on seasonal variation of dust emission and dust optical depth near the source regions. Globally, we have found that the permanent bare land contributes to 88% of the total dust emission, whereas the grassland and cultivated crops land contribute to about 12%. Our results suggest the potential of using NDVI over a vegetated area to link the dust emission with land cover and land use change for air quality and climate change studies.

Citation: Kim, D., M. Chin, H. Bian, Q. Tan, M. E. Brown, T. Zheng, R. You, T. Diehl, P. Ginoux, and T. Kucsera (2013), The effect of the dynamic surface bareness on dust source function, emission, and distribution, *J. Geophys. Res. Atmos.*, *118*, 871–886, doi: 10.1029/2012JD017907.

1. Introduction

[2] Dust is one of the most prominent aerosol types in the atmosphere, which plays an important role in the Earth climate system [*Forster et al.*, 2007]. Numerous studies have shown the importance of dust to affect the Earth's radiation budget, atmospheric dynamics, atmospheric chemistry, air quality, and ocean biogeochemistry over wide ranges of spatial and temporal scales [*Husar et al.*, 2001; *Haywood et al.*, 2005; *Jickells et al.*, 2005].

[3] Soil particle mobilization into the atmosphere is driven mainly by the winds. In the numerical models, such process is often parameterized as a function of the friction wind (u^*) or near-surface wind speed [e.g., *Tegen and Fung*, 1995; *Ginoux et al.*, 2001; *Zender et al.*, 2003; *Textor et al.*, 2006; Huneeus *et al.*, 2011]. Other factors affecting dust mobilization include soil moisture (or surface wetness) and vegetation cover (surface roughness), as dust is usually uplifted over dry surfaces with little vegetation coverage. The variations of these factors are very different in terms of time scales, for example winds vary subhourly, soil moisture daily to seasonally, and surface bareness seasonally to interannually. While all models explicitly take into account the change of wind speed and soil moisture in calculating dust emissions, they commonly

[1]JCET, University of Maryland, Baltimore County, Baltimore, Maryland, USA.
[2]NASA Goddard Space Flight Center, Greenbelt, Maryland, USA.
[3]Universities Space Research Association, Columbia, Maryland, USA.
[4]Montgomery Blair High School, Silver Spring, Maryland, USA.
[5]Department of Mechanical Engineering, University of Maryland, College Park, Maryland, USA.
[6]Thomas Jefferson High School for Science and Technology, Alexandria, Virginia, USA.
[7]Department of Mathematics, Stanford University, Stanford, California, USA.
[8]Geophysical Fluid Dynamics Laboratory, NOAA, Princeton, New Jersey, USA.

Corresponding author: D. Kim, JCET, University of Maryland, Baltimore County, Baltimore, MD 21250, USA. (dongchul.kim@nasa.gov)

©2012. American Geophysical Union. All Rights Reserved.
2169-897X/13/2012JD017907

employ a "climatological" land cover data for identifying dust source locations and neglect the time variation of surface bareness [e.g., *Ginoux et al.*, 2001; Huneeus *et al.*, 2011]. Although such an approach is adequate over permanent desert locations because of little vegetation coverage there, the static dust source does not reflect the dynamic land cover changes over other areas and could cause significant error in estimating dust emissions in some seasons.

[4] In this study, we investigate the effects of temporal variation of surface bareness on seasonal cycles of dust emissions and atmospheric loading. We use the satellite data from normalized difference vegetation index (NDVI) from the advanced very high resolution radiometer (AVHRR) to construct a dynamic dust source function map at 15 day time resolution, and apply this source function to the dust simulation with the Goddard Chemistry Aerosol Radiation and Transport (GOCART) model. Previous studies have shown that there is a statistically significant relationship between NDVI and dust loading in source regions [*Zender and Kwon*, 2005] and time-changing vegetation coverage data can significantly improve dust emission process [*Tegen et al.*, 2002; *Fairlie et al.*, 2007; *Webb and McGowan*, 2009; *Shannon and Lunt*, 2011]. Some regional models have used the NDVI information to produce a continuous weighting function for dust emission [*Park et al.*, 2010]. Our study here provides an analysis of such effects on dust regions over the globe from 2000 to 2007, and then compares this dynamic source with the static source function in previous GOCART model simulations to assess the significance.

[5] In section 2, we will describe how our time resolved surface bareness map is constructed from the satellite observed NDVI. We will present the relationship among NDVI, the surface bareness, and dust source function in various source regions. We will investigate the time-dependent dust source function in section 3 and its effect to the dust emission and distribution using the GOCART model and compare the simulated aerosol optical depth with satellite and surface measurement data in section 4. Discussion and summary are given in sections 5 and 6, respectively.

2. Method

2.1. General

[6] Dust uplifting to the atmosphere occurs mainly by sand blasting or soil bombardment, which is parameterized in GOCART assuming that the vertical particle flux is proportional to the horizontal wind flux [*Ginoux et al.*, 2001]. The emission parameterization requires the knowledge of the 10 m wind speed, the threshold velocity of wind erosion, and the surface condition for each dust size class. Dust emission flux E_p (μg m^{-2} s^{-1}) for a size group p is expressed as

$$E_p = C \times S \times s_p \times u^2{}_{10} \times (u_{10} - u_t), if\, u_{10} > u_t \qquad (1)$$

where C is a dimensional factor (1 μg s^2 m^{-5}), S is the dust source function or probability of dust uplifting with a value between 0 and 1, s_p is the fraction of size group p within the soil [*Tegen and Fung,* 1995], u_{10} is the 10 m wind speed (m s^{-1}), and u_t is the threshold velocity of wind erosion as a function of dust density, particle diameter, and surface wetness to account for the bonding effect between water and particles [*Ginoux et al.*, 2001, 2004]. Two soil types are considered for erosion: clay (particle radius less than 1 μm) and silt (particle radius greater than 1 μm and less than 10 μm),

[7] The dust source function S is determined by the surface bareness (B) and topographical depression features (H). Here, H is calculated from the elevation of the grid cell relative to the elevation of the surrounding areas [*Ginoux et al.*, 2001] (equation (2)). This method is based on the consideration that dust sediments from surface erosion are accumulated in valleys and depressions.

$$H = \left(\frac{z_{\max} - z_i}{z_{\max} - z_{\min}}\right)^5 \qquad (2)$$

where H is the probability to have accumulated sediments in a grid cell i of altitude z_i. Here z_{max} and z_{min} are the maximum and minimum elevations of $10° \times 10°$ topography. Fifth-order power is applied to increase the topographic contrast.

[8] In previous GOCART simulations [e.g., *Ginoux et al.*, 2001, 2004; *Chin et al.*, 2002, 2009], the surface bareness B was determined based on the 1987 annual averaged satellite land cover data from AVHRR [*DeFries and Townshend*, 1994], which does not change with time. Although such constructed dust source collocates with the satellite observed dust "hot spots" [e.g., *Ginoux et al.*, 2001; *Prospero et al.*, 2002], it is a static function (denoted as S_{Static} hereafter) that neither reflects the land cover change nor considers seasonal variations of soil bareness. This study therefore focuses on improving the seasonal and interannual variation of dust source function, as described in the next sections.

2.2. Time-Dependent Surface Bareness

[9] In this study, we utilized the AVHRR NDVI composite from the NASA Global Inventory Monitoring and Modeling Systems (GIMMS) [*Tucker et al.*, 2005; *Brown et al.*, 2006]. We used the AVHRR sensor instead of the data from MODIS because of its longer record. AVHRR data is available from 1981 to 2008, and will soon be extended to 2012. Although here we use the NDVI only during eight years in the MODIS period, we develop this method so that the model can be run over the longer time period.

[10] The GIMMS data have been corrected to reduce the influence of water vapor due to the wide spectral bands in AVHRR [*Tucker et al.*, 2005]. We only used quality assured data to reduce possible noise from unexpected surface conditions. Satellite drift correction has been applied to this data set to further remove artifacts due to orbital drift and changes in the Sun-target-sensor geometry [*Pinzon et al.*, 2005].

[11] NDVI is calculated from the visible (VIS) and near-infrared (NIR) light reflected by vegetation [*Tucker*, 1979]:

$$NDVI = (NIR - VIS)/(NIR + VIS) \qquad (3)$$

NDVI is usually very low when the ground is bare and gets higher as ground is covered by more vegetation. Here, we choose a threshold NDVI value of 0.15, below which the surface is considered to be bare. This threshold will vary depending on the data set used due to each sensor's unique design and sensitivity to vegetation [*Brown et al.*, 2006].

[12] Using the 8 km spatial resolution AVHRR NDVI data ($NDVI_{8km}$) and the bareness threshold NDVI value, we have constructed a global surface bareness (B) map in $1° \times 1°$

spatial resolution from 1981 to 2008 with the same time resolution as the AVHRR NDVI data at two times per month. In each $1^\circ \times 1^\circ$ grid cell, B is calculated as the ratio of the number of $NDVI_{8km}$ pixels that are below 0.15 (i.e., $N_{<0.15}$) to the total number of $NDVI_{8km}$ pixels within the grid cell (i.e., N_{total}; equation (4)). In reality, different bare surface should have different reflectance, and ideally the threshold NDVI should be variable determined by the characteristics of the bare surface, such as soil composition or surface roughness. However, currently there are no available best estimates on the spatially varying threshold NDVI. This value was chosen based on several observations over various desert surfaces that is around 0.15 [*Tucker et al.*, 1991; *Peters and Eve*, 1995; *Sobrino and Raissouni*, 2000; *Bradley and Mustard*, 2005].

$$B = \frac{N_{<0.15}}{N_{total}} \tag{4}$$

[13] The 8 year mean global distributions of NDVI and B are shown for January and July (Figure 1). High NDVI appears in densely vegetated areas such as in Amazon and South Africa, and low NDVI appears in desert regions such as Sahara and Middle East. The constructed B map shows little seasonal variability in desert belt regions, i.e., Saharan, Arabian, and China Deserts, but in other dry regions it reveals stronger seasonal changes.

3. Dust Source Function

3.1. Seasonal Variations

[14] The new dust source function is constructed using the aforementioned time resolved soil bareness and topographic features to identify the probability of location and time of dust uplifting. The 10 min topography map from the Navy Fleet Numerical Oceanography Center, Monterey [*Prospero et al.*, 2002] is used to construct the H in equation (2). In addition, we utilize other data to further mask the nondust areas, including the land cover from AVHRR [*Hansen et al.*, 2000] to mask the forest area and the soil depth data from the Food and Agriculture Organization of the United Nations to screen out the nonsoil bare areas (i.e., soil depth less than 10 cm) (http://www.fao.org/nr/land/soils/en/). We also exclude the bare surfaces covered by snow or with temperature below 260°K as dust source locations (Figure 2).

[15] Figures 3a–c shows the new dynamic source function ($S_{dynamic}$) in January and July averaged from 2000 to 2007 and the July-to-January ratio. While there is little seasonal variation over the Saharan, Arabian, and Taklimakan deserts, $S_{dynamic}$ varies with a magnitude often greater than a factor of 2 in many other source regions such as Sahel, Somalia, Thar desert, Western US, Chile, Australia, and South Africa (Figure 3c). For comparison, Figures 3d–f shows the previously used static source function (S_{static}, Figure 3d) and the ratio of $S_{dynamic}$ to S_{static} for January

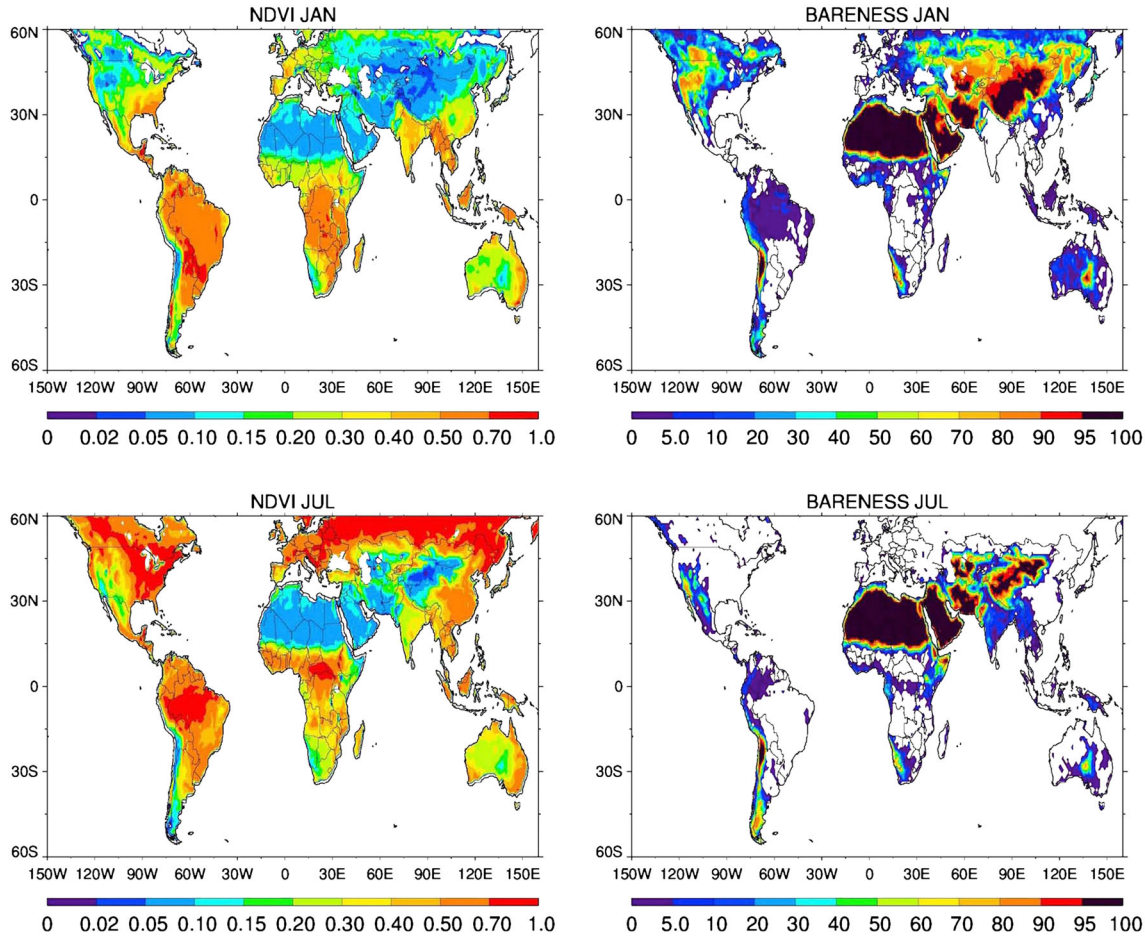

Figure 1. Mean AVHRR NDVI and bareness (%) map for January and July averaged from 1981 to 2007.

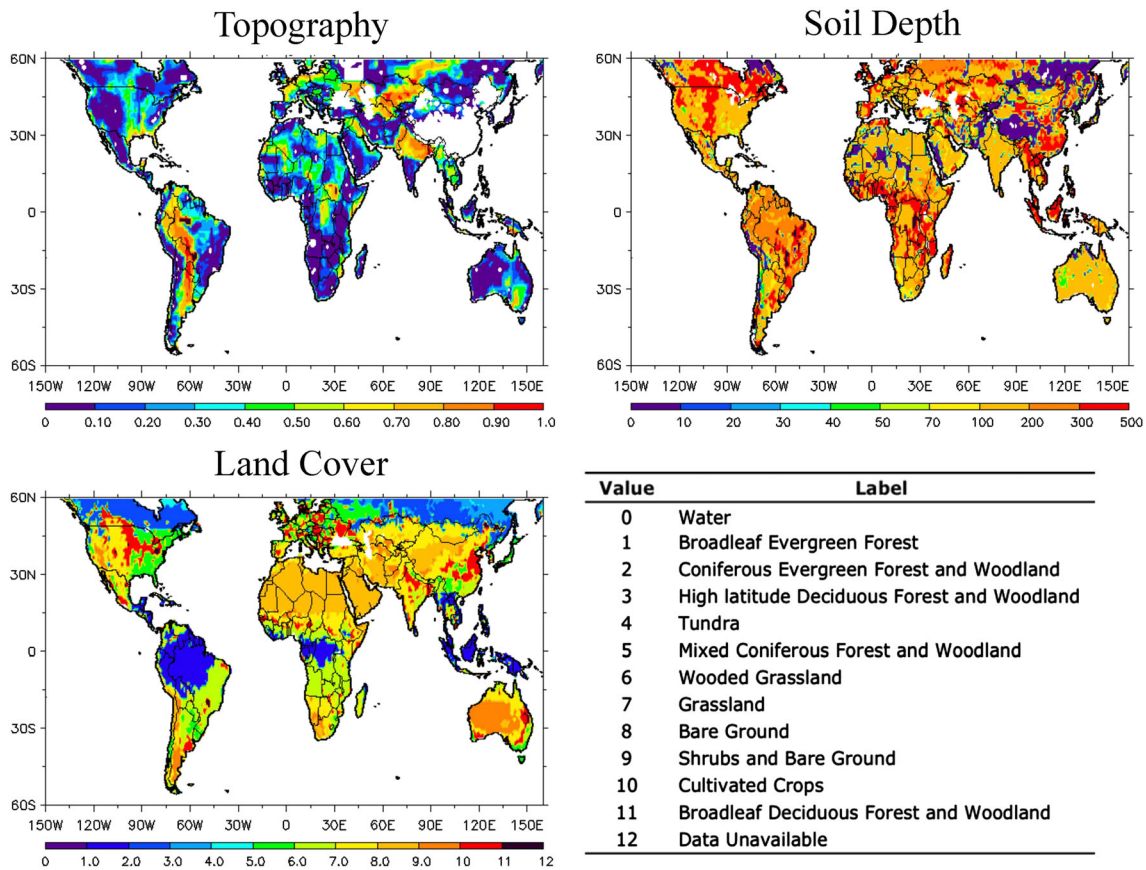

Value	Label
0	Water
1	Broadleaf Evergreen Forest
2	Coniferous Evergreen Forest and Woodland
3	High latitude Deciduous Forest and Woodland
4	Tundra
5	Mixed Coniferous Forest and Woodland
6	Wooded Grassland
7	Grassland
8	Bare Ground
9	Shrubs and Bare Ground
10	Cultivated Crops
11	Broadleaf Deciduous Forest and Woodland
12	Data Unavailable

Figure 2. Global distribution of topographical depression (H, dimensionless), soil depth (cm), and land cover classification.

(Figure 3e) and July (Figure 3f). Even though qualitatively both $S_{dynamic}$ and S_{static} show similar high values in the Afro-Asian dust belt region and moderate to low values in other source regions (Figures 3a, b, and d). $S_{dynamic}$ is often different from S_{static} by a factor of 2 or more in many locations, such as Gobi desert, Karakum (east of Caspian Sea), Australia, and South America where $S_{dynamic}$ is higher and some part of Saharan desert, Chotts, and Southern Gobi desert where $S_{dynamic}$ is lower (Figures 3d and f).

3.2. Relationship Between Dust Source Function, Surface Bareness, and Topographic Features

[16] Locations of major global dust source regions have been identified in previous studies using different criteria. For example, *Prospero et al*. [2002] used the TOMS aerosol index data and *Koven and Fung* [2008] used various erodibility indices including topography, inverse elevation, NDVI, surface roughness, and hydrologic state to recognize major source locations over the globe. In this study, we have selected 22 dust source regions based on both *Prospero et al*. [2002] and *Koven and Fung* [2008] to analyze their seasonal variations. Geographical information of each region and its location are given in Table 1 and Figure 4. Note that our selected domain areas are not exactly the same as those in the previous studies since we included the NDVI data in determining desert emission area. The NDVI map of the selected dust source regions shows the heterogeneous land cover in the source region and its seasonality (Figure 5). Some are "permanent desert" (i.e., NDVI is less than 0.15 throughout year), such as Sahara, Arabia, Taklimakan, and Gobi deserts in group I. The mean NDVI in these deserts is around 0.1, far below our threshold value of 0.15. Other deserts have more seasonally variable NDVI (i.e., NDVI < 0.15 only during dry season), such as Sahel, Australia, Chinese Loess, South and North America, South Africa in groups II and III, where the driest part of those region is almost always lower than 0.15 but the surrounding area has strong seasonal variability.

[17] The source function–related parameters, emission, and aerosol optical depth of the considered source area are summarized in Table 2. As we indicated earlier, the source function S represents the probability of dust uplift, which depends on the degree of both bareness (B) and surface depressions (H). There is a wide the range of B and H, depending on source regions. We divide the 22 source regions into three groups according to the strength of B and H. Group I consists of permanent deserts, such as Bodélé and Arabian desert (Chotts), with high values of H and low variability of B. Almost half of the analyzed source regions fall into group I. The remaining regions have different degree of seasonal variation of B. For those regions, we select the more active ones with high degree of H (>0.1) in group II, such as Thar, Lake Eyre, and Somalia, and less active ones with low H (<0.1) in group III, such as Namibia, Mexico, and Salt Lake.

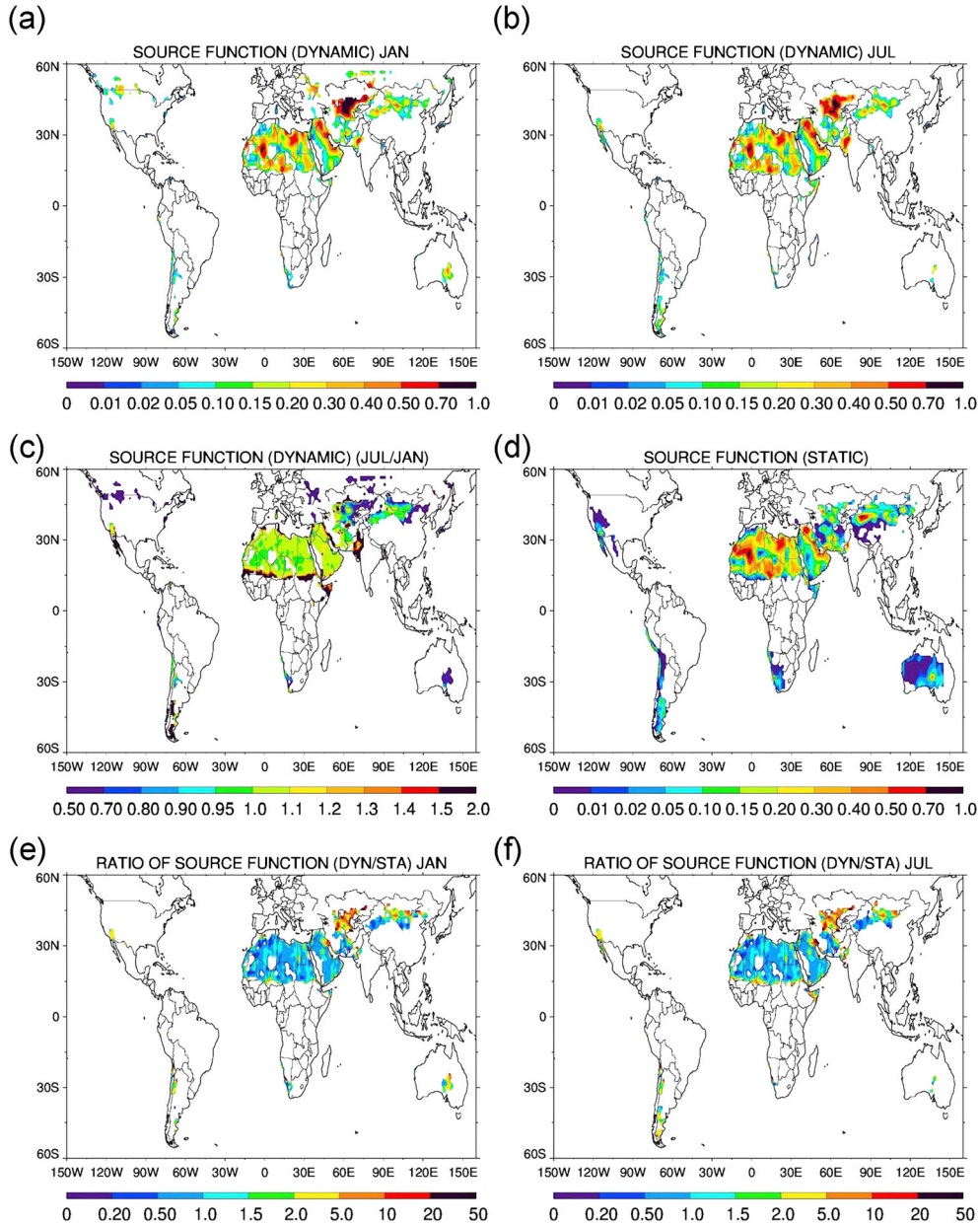

Figure 3. Distribution of static and dynamic source function and the differences between the two. Dynamic source function is averaged for January and July from 2000 to 2007.

[18] We examine the relationship between S, B, and H for selected dust regions and illustrate it in Figure 6. The most distinctive characteristics in group I is the high percentage of bareness (>0.88) throughout the year. In group I, both dynamic and static bareness are constantly high throughout the year. Topography depression H that affects to the emission efficiency varies by deserts, i.e., 0.4 in Bodélé and 0.2 in Gobi. Bareness in groups II and III varies significantly from below 0.2 to above 0.9 depending on seasons, with an annual mean about 0.56. However, the behavior of $S_{dynamic}$ between group II and III is quite different. The $S_{dynamic}$ in group II varies significantly with time; the differences between the maximum and minimum values are as large as 0.4, 0.3, and 0.1 in Thar Desert, Lake Eyre, and Somalia Desert, respectively. The relatively large H (between 0.2 and 0.8) combined with the time-varying B results a substantial seasonality of the $S_{dynamic}$ in group II. In contrast, the seasonal change and the values of $S_{dynamic}$ in group III are much less than those in group II despite the large seasonal change of B, due to the low degree of H in group III that damper the magnitude of seasonal variations and determine the low values of $S_{dynamic}$.

4. Simulation of Dust Aerosol With Dynamic Source Functions

[19] With the new $S_{dynamic}$, we use the GOCART model to simulate dust emissions and atmospheric distributions. GOCART is driven by the assimilated meteorological fields from the Goddard Earth Observing System Data Assimilation System (GEOS DAS) [*Ginoux et al.*, 2001; *Chin et al.*, 2002, 2009; *Bloom et al.*, 2005]. In the GOCART

Table 1. Name and Location of Dust Source Regions

Number	Name	Boundary	Group[a]
1	Karakum	54.0°E–65.0°E, 37.0°N–42.0°N	I
2	Argentina	70.0°W–67.0°W, 33.0°S–30.0°S	I
3	Bodel	10.0°E–20.0°E, 15.0°N–20.0°N	I
4	Chile	71.0°W–67.0°W, 28.0°S–19.0°S	I
5	Chotts	5.0°E–10.0°E, 32.0°N–35.0°N	I
6	Gobi	100.0°E–105.0°E, 42.5°N–45.0°N	I
7	Nile	29.0°E–34.0°E, 28.0°N–31.0°N	I
8	Oman	52.5°E–57.5°E, 18.0°N–21.0°N	I
9	Saudi Arabia	47.5°E–52.5°E, 20.0°N–25.0°N	I
10	Tarim Basin	75.0°E–90.0°E, 35.0°N–40.0°N	I
11	Tigris	42.5°E–57.5°E, 28.0°N–32.0°N	II
12	China Loess	103.0°E–110.0°E, 36.5°N–39.0°N	II
13	Lake Eyre	136.0°E–140.0°E, 30.0°S–25.0°S	II
14	Mojave	116.0°W–113.0°W, 32.0°N–35.0°N	II
15	Patagonia	72.0°W–68.0°W, 51.0°S–43.0°S	II
16	Sahel	0.0°E–20.0°E, 13.0°N–16.0°N	II
17	Somalia	45.0°E–51.0°E, 8.0°N–11.5°N	II
18	Thar	70.0°E–74.0°E, 25.0°N–29.0°N	II
19	Mexico	108.0°W–103.0°W, 29.0°N–33.0°N	III
20	Namibia	15.0°E–19.0°E, 29.0°S–23.0°S	III
21	Salt Lake	115.0°W–112.0°W, 39.0°N–42.0°N	III
22	Botswana	24.0°E–27.0°E, 22.0°S–19.0°S	III

[a]Type of desert groups defined in this study.

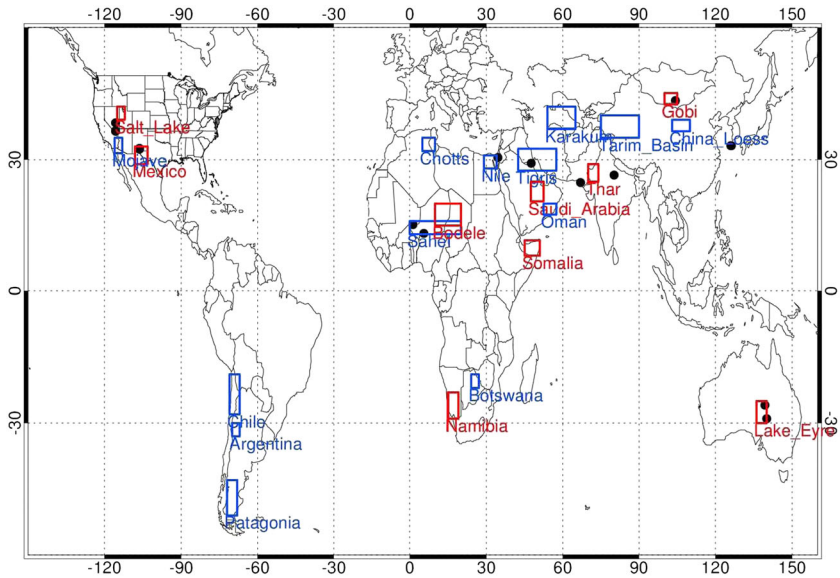

Figure 4. Location of the 22 dust source regions selected for the analysis. Regions for the in-depth analysis are in red boxes, and black dots indicate the location of AERONET sites.

model, aerosol advection is computed by a flux form semi-Lagrangian method that is a second-order closure scheme for the boundary layer turbulent mixing and the moist convection is based on the cloud mass flux fields. Dry deposition includes gravitational settling as a function of aerosol particle size and air viscosity and surface deposition as a function of surface type and meteorological conditions [*Fuchs*, 1964; *Wesely*, 1989]. Wet deposition accounts for the scavenging of soluble species in convective updrafts and rainout/washout in large-scale precipitation [*Giorgi and Chameides*, 1986; *Balkanski et al.*, 1993]. Radiative calculation is based on OPAC data set [*Hess et al.*, 1998]. Dust particle size distribution is described by eight size bins is in the size range from 0.1 to 10 μm in radius to take into account size-dependent physical and optical processes. The eight size bins that describe size range are 0.1–0.18, 0.18–0.3, 0.3–0.6, 0.6–1, 1–1.8, 1.8–3, 3–6, and 6–10 μm [*Chin et al.*, 2009]. The horizontal resolution of the model is 1° latitude by 1.25° longitude with 30 vertical sigma layers up to 10 hPa. In the present study two dust simulations are conducted from January 2000 to December 2007, where the first simulation is with the static source function [*Ginoux et al.*, 2001] and the other with the new dynamic source function.

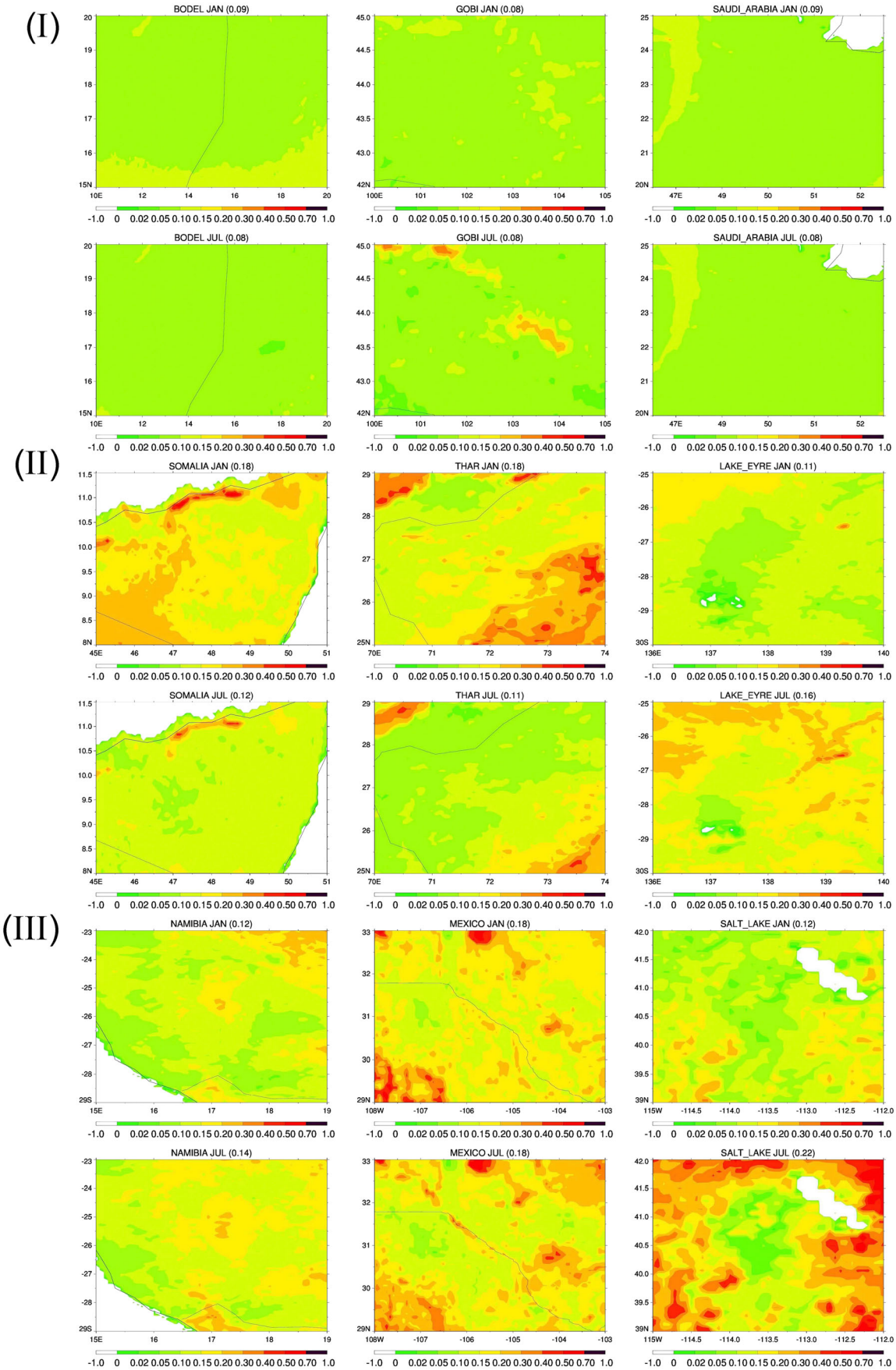

Figure 5. Mean NDVI map in various source regions in January and July, averaged from 2000 to 2007.

Table 2. Mean Variables of Regional Average NDVI, Surface Bareness (*B*), Degree of Topographic Depression (*H*), Source Function (*S*), 10 m Wind Speed (u10), Annual Emission (EMI), and AOD Over 22 Desert Regions Averaged From January 2000 to December 2007[a]

Group	Name	NDVI	B	H	S	u10	EMI (mg m^{-2} d^{-1})	Modeled AOD	Satellite AOD
I	Karakum	0.08	76.15	0.68	0.46 (0.13)	4.16	529.4 (132.4)	0.31 (0.16)	0.19 [0.25]
I	Argentina	0.08	41.71	0.36	0.06 (0.03)	4.82	139.2 (65.9)	0.02 (0.02)	0.09 [0.15]
I	Bodel	0.01	99.71	0.43	0.35 (0.42)	5.49	1035.3 (1067.3)	0.49 (0.55)	0.49 [0.54]
I	Chile	0.01	84.12	0.09	0.06 (0.08)	4.62	119.6 (93.2)	0.02 (0.02)	0.11 [0.17]
I	Chotts	0.06	56.44	0.32	0.20 (0.30)	4.50	369.8 (443.3)	0.30 (0.31)	0.27 [0.32]
I	Gobi	0.06	88.44	0.21	0.17 (0.07)	4.30	233.0 (167.0)	0.13 (0.13)	0.15 [0.12]
I	Nile	0.05	66.23	0.41	0.32 (0.28)	4.56	544.4 (381.3)	0.25 (0.21)	0.23 [0.31]
I	Oman	0.01	94.94	0.15	0.13 (0.12)	4.66	204.5 (155.9)	0.25 (0.20)	0.37 [0.26]
I	Saudi Arabia	0.01	89.49	0.29	0.26 (0.26)	4.32	373.0 (305.6)	0.33 (0.27)	0.43 [0.31]
I	Tarim Basin	0.04	88.21	0.17	0.13 (0.16)	4.78	290.6 (881.3)	0.17 (0.35)	— [0.39]
II	Tigris	0.04	75.88	0.32	0.23 (0.15)	4.45	290.5 (209.6)	0.28 (0.22)	0.25 [0.27]
II	China Loess	0.16	65.51	0.11	0.06 (0.16)	4.13	94.9 (385.7)	0.14 (0.20)	0.24 [0.23]
II	Lake Eyre	0.07	55.69	0.38	0.21 (0.14)	4.31	282.4 (194.5)	0.04 (0.03)	0.11 [0.15]
II	Mojave	0.06	47.73	0.36	0.17 (0.08)	3.87	157.5 (77.3)	0.05 (0.04)	0.11 [0.30]
II	Patagonia	0.14	43.00	0.24	0.08 (0.04)	6.16	289.1 (203.3)	0.01 (0.01)	0.06 [0.19]
II	Sahel	0.08	73.46	0.40	0.21 (0.20)	4.74	556.6 (427.3)	0.54 (0.55)	0.47 [0.62]
II	Somalia	0.02	48.45	0.24	0.14 (0.06)	6.48	758.3 (297.1)	0.16 (0.08)	0.27 [0.31]
II	Thar	0.17	37.48	0.77	0.37 (0.25)	3.55	379.0 (200.5)	0.22 (0.16)	0.39 [0.59]
III	Mexico	0.11	21.58	0.08	0.01 (0.01)	4.21	14.1 (10.2)	0.02 (0.02)	0.13 [0.17]
III	Namibia	0.06	52.95	0.09	0.08 (0.07)	4.61	123.6 (137.7)	0.02 (0.02)	0.12 [0.15]
III	Salt Lake	0.33	27.86	0.03	0.01 (0.00)	4.18	5.7 (5.0)	0.03 (0.03)	0.12 [0.16]
III	Botswana	0.30	4.10	0.10	0.01 (0.00)	3.83	7.1 (0.0)	0.00 (0.00)	0.17 [0.16]

[a]Model-calculated emission and AOD by static source function are shown in parentheses. Satellite AOD from MISR and MODIS Deep Blue (in brackets) are also listed.

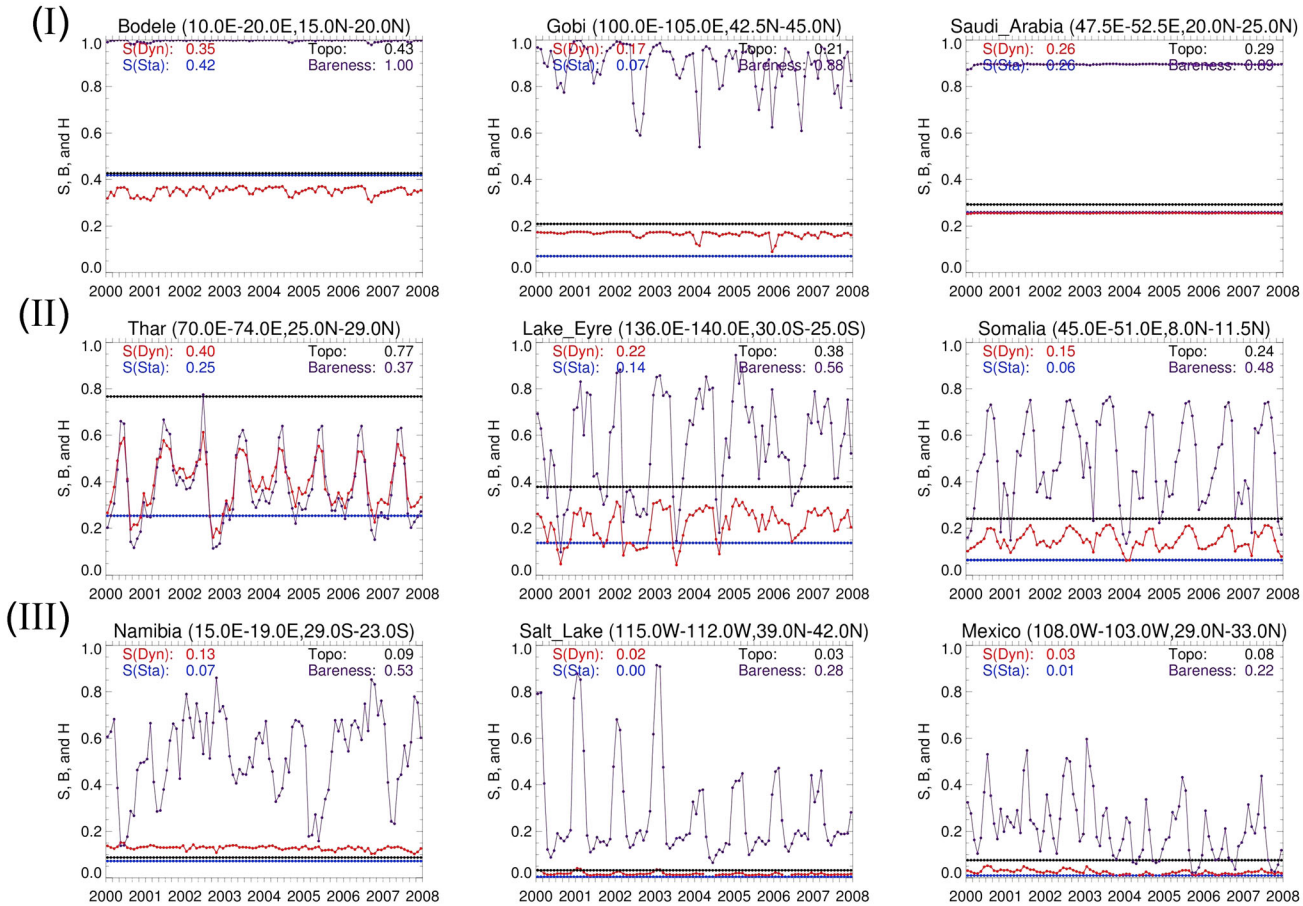

Figure 6. Time series of monthly mean dynamic (red) and static (blue) source functions (*S*), topographic depression (*H*, black), and surface bareness (*B*, purple). Numbers in each panel are monthly mean of each variable.

4.1. Dust Emissions With Dynamic and Static Source Functions

[20] The monthly mean dust emission using both S_{static} and $S_{dynamic}$ are plotted for January and July averaged from 2000 to 2007 (Figure 7). Even though most active dust source appears in the dust belt, other hot spots appear to produce significant amount of dust in both static and dynamic source function simulations. Dust emission shows a wide

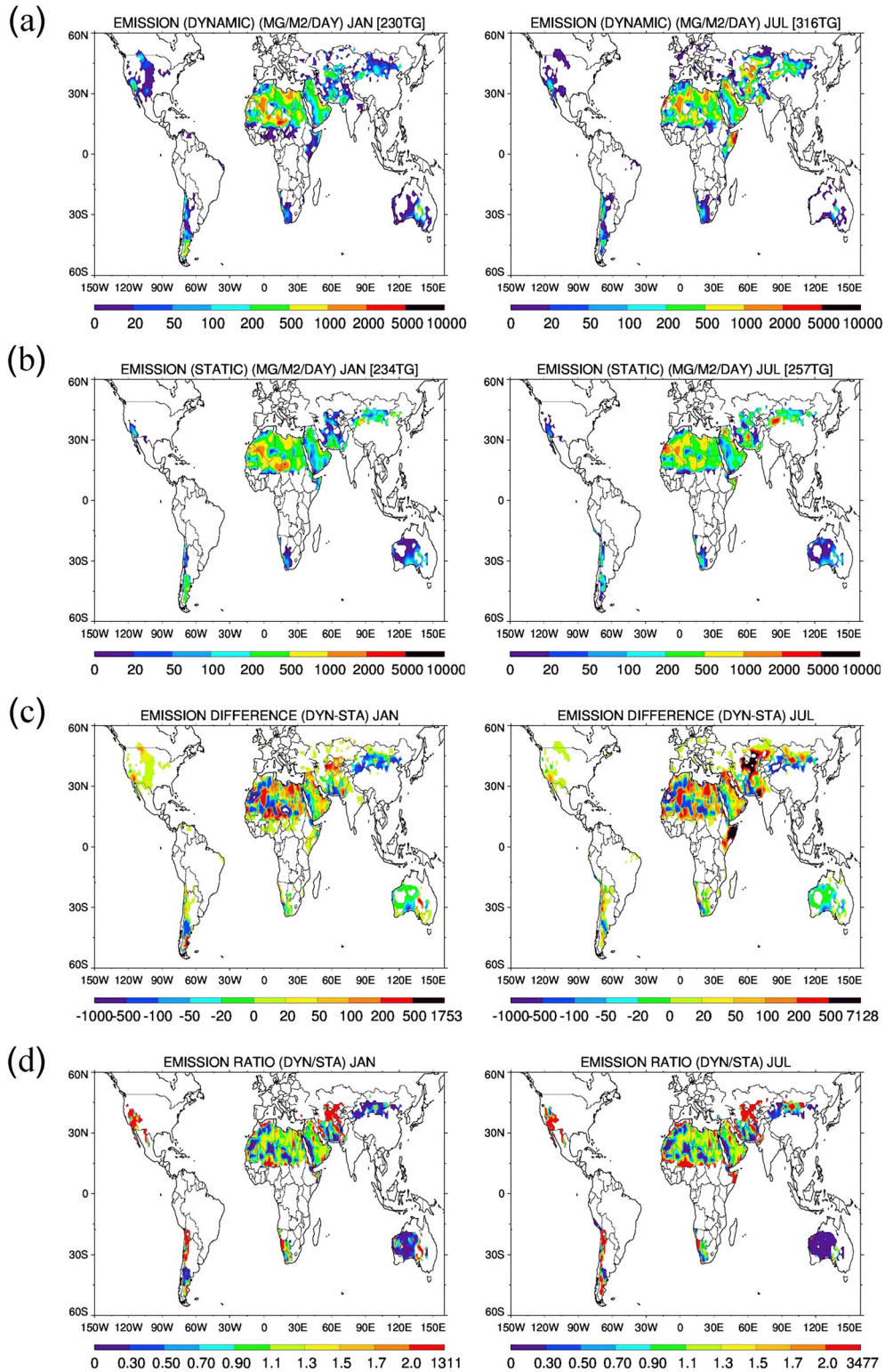

Figure 7. Monthly mean emission for January and July using a (a) dynamic source function and (b) static source function. (c) Absolute and (d) relative difference in emission between dynamic and static source maps. All plots are averaged in the period from 2000 to 2007.

range from 100 to 5000 mg m^{-2} d^{-1} with strong seasonality in most emission regions. The effect of $S_{dynamic}$ over S_{static} is more obvious with the absolute and relative differences between two methods (Figures 7c and d). The absolute difference of emissions is strongest in dust belt throughout year in the range between -500 and +500 (g m^{-2} d^{-1}). The $S_{dynamic}$ appears to produce a factor of two more dust emission than the S_{static} in several source regions including North America, Chile, central Asia (Karakum Desert), and Sahel. Dust emission is reduced in some source areas such as Patagonia and China. The global total dust emission is 3245 Tg/yr with $S_{dynamic}$ and 2985 Tg/yr with S_{static}, resulting 8.7% higher emission in the dynamic source function. The emission in each region is summarized in Table 2.

[21] As equation (1) shows, the 10 m wind speed (u10) is the driving force for dust emission that is proportional to the third power of u10. Other parameters, including the surface bareness B, exert modulating effects. We compared dust emissions as a function of u10 with $S_{dynamic}$ and S_{static} in nine selected source regions (three for each group) in Figure 8. Since same meteorological fields are used for the simulation, the range of u10 is the same in two simulations. As expected, dust emissions from both source functions are well correlated with u10. The largest difference in emission amount between simulations with $S_{dynamic}$ and S_{static} appears in group II (Figure 8, middle), where the emission with $S_{dynamic}$ is up to a factor of 2 higher than that with S_{static}. The difference of dust emission in group I regions (Figure 8, top) varies with locations; for example, the emissions are nearly identical in Bodélé but the difference is about 50% in Gobi and 20% in Saudi Arabian deserts (emission being higher with $S_{dynamic}$). In comparison, regions in group III (Figure 8, bottom) are generally less active with lower emissions rates and there are only marginal differences between the simulations with two different source functions.

[22] The major difference between $S_{dynamic}$ and S_{static} is that S_{static} only considers the dust emissions from the bare ground but $S_{dynamic}$ includes dust emissions from other areas that can be covered by vegetation during growing seasons. To estimate the dust emission from both bare and vegetated land cover areas with $S_{dynamic}$, we grouped 12 land cover classes in Figure 2 into two categories of bare land (bare ground and shrubs and bare ground in Figure 2) and vegetated land (the remaining land types). On a global annual average between 2000 and 2007, 88% (2861 Tg/yr) of dust are emitted from the bare land, and 12% (384 Tg/yr) from vegetated land (Figure 9). Three land types of wooded grassland, grassland, and cultivated crop land contribute to 0.2%, 10.2%, and 1.0% of dust emission, respectively.

4.2. Comparisons of Dust AOD With Observations

[23] We compare model simulated AOD with observations from satellite sensors of the Multiangle Imaging Spectroradiometer (MISR) and the Moderate Resolution

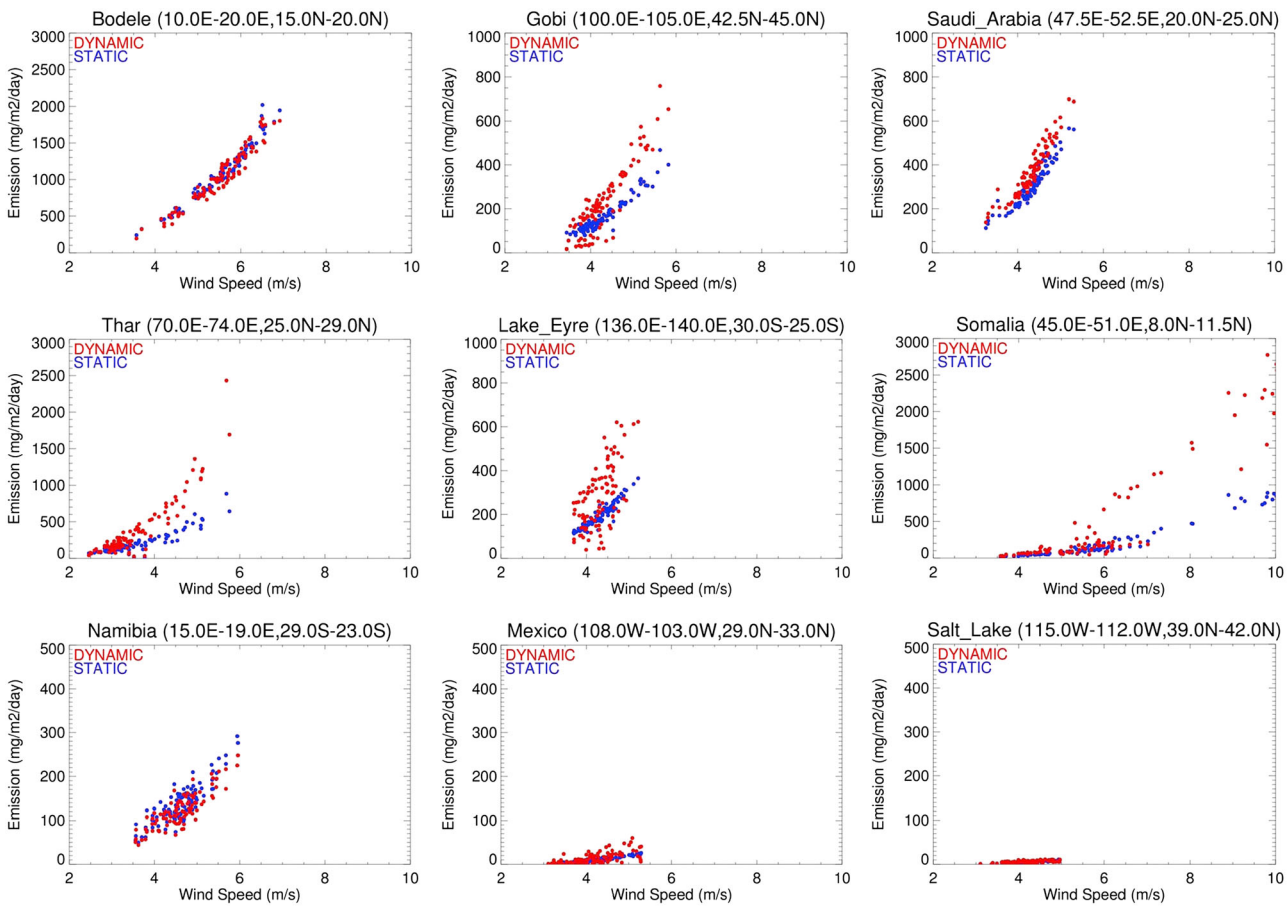

Figure 8. Relationships between emission and u10. Each dot is monthly mean values over the domain.

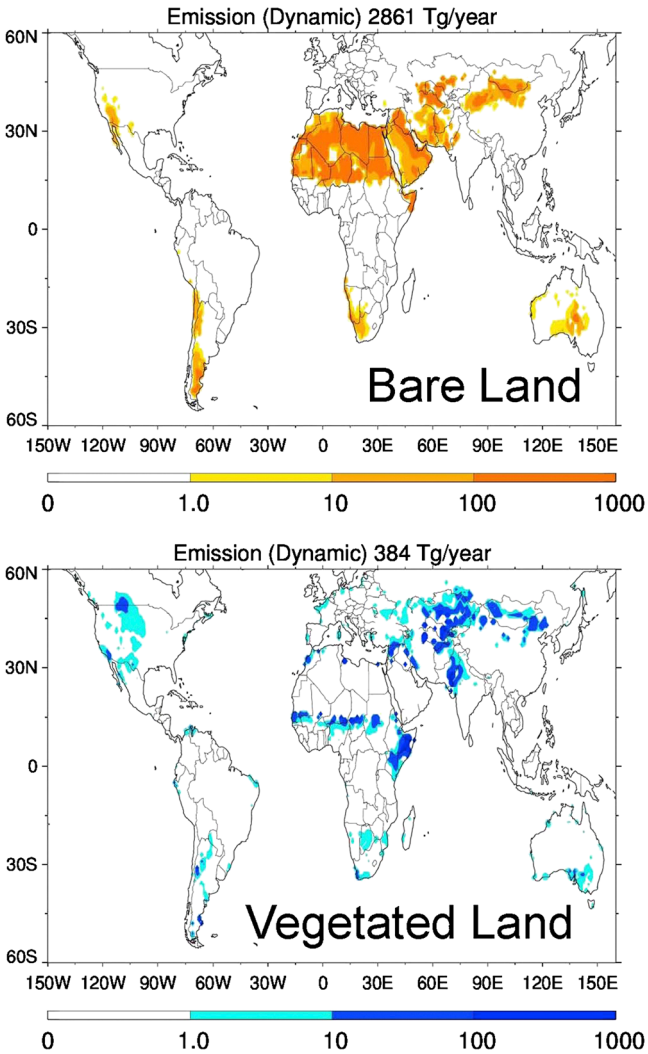

Figure 9. Dust emission from (top) bare land and (bottom) vegetated land. Plots are averaged in the period from 2000 to 2007.

Imaging Spectroradiometer (MODIS), and from ground-based Sun photometer measurements of the Aerosol Robotic Network (AERONET). AERONET [*Holben et al.*, 1998] was established in the 1990s and currently consists of more than 200 sites over the globe. It provides direct measurement of AOD at multiple wavelengths from near UV to near IR during daytime with an uncertainty of 0.01–0.02 at the visible wavelength. The MODIS instruments aboard the NASA Earth Observing System (EOS) Terra and Aqua satellites provide aerosol related parameters for the entire globe since 2000 and 2002, respectively. Along with the standard MODIS AOD product over relatively dark surfaces of land and ocean [*Remer et al.*, 2005; *Levy et al.*, 2010], the Deep Blue algorithm applied to Aqua retrieves AOD at 550 nm over bright land surfaces such as desert [*Hsu et al.*, 2004]. The Deep Blue algorithm uses two blue channels of 0.412 μm and 0.470 μm, where surface reflectance is relatively small and their uncertainty is in the range of 25–30% when it is compared with AERONET sites in Asian desert [*Hsu et al.*, 2006]. MISR is a multiangle multispectral instrument onboard Terra [*Kahn et al.*, 1998, 2001]. MISR validation study shows that the uncertainty of retrieved AOD is within ±0.05 or 20% compared to AERONET [*Kahn et al.*, 2005]. Another comparison study with AERONET in desert regions estimates that the estimated uncertainty of MISR AOD is 0.05–0.08 in visible wavelength [*Martonchik et al.*, 2004]. We use the Level 2 (version 2) monthly average data between 2000 and 2007 at sites over the major dust source regions. In this study, the satellite data are gridded to $1^\circ \times 1^\circ$ to be consistent with the model spatial resolution. All the comparisons are done with the AOD at 550 nm.

[24] Figure 10 compares the AOD from MISR (first column) and MODIS Deep Blue (second column) with two model simulations using $S_{dynamic}$ (third column) and S_{static} (fourth column) for July which is an active dust month. Here we include all aerosols simulated with GOCART (sulfate, black carbon, organic matter, dust, and sea salt) for more appropriate comparisons to total AOD from satellite. However, the differences of AOD in these two model simulations (third and fourth columns in Figure 10) are entirely due to the dust AOD simulated with different source functions. Although the seasonal variation patterns and the geographical distributions are similar, there are as much as factor of 2 differences in AOD between MISR and MODIS Deep Blue, depending on region and season. For example, MODIS Deep Blue AOD is 10% (Somalia) to factor of 3 (Thar desert) higher than MISR in July. The modeled AOD with the dynamic source function is from 40% (Thar desert and Tigris) to twice (Somalia and Karakum Desert) larger than the static source function simulation. Since the AOD from the static source function in general underestimates than the observed AOD, the increase of AOD in the dynamic source function indicates the improved AOD by the new source function.

[25] Time series of the monthly mean total AOD from the model simulations are plotted along with the satellite observed AOD from MISR and MODIS Deep Blue in 9 selected regions (Figure 11). During the peak season (July), simulated AOD from $S_{dynamic}$ and S_{static} are similar in Bodélé and Gobi but are significantly different as much as factor of 2 in other regions, while the difference in January is less than 10%. The correlation coefficients between modeled and MISR AODs are 0.71–0.90 in groups I and II, but the range is 0.46–0.68 in group III. There is no significant change between model results with S_{dynmic} and S_{static} in group I, because these are permanent deserts with similar emission rates. In group II, the dynamic source function simulation enhances AOD as expected from the emission comparison and the dynamic source function run is better agreed with satellite in peak AOD season. The dynamic source function shows better statistical performance than the static source function, i.e., the correlation coefficient is increased about 0.1 and the mean bias is reduced 0.1–0.3. Sahel region has strong seasonality in bareness and falls in group II. It has high source function but the lower emission due to the weaker wind speed which is similar to the previous study by *Ginoux et al.* [2010]. In group III, dust AOD from two model simulations is much lower than satellite observation indicating that model has large discrepancies with observations in the region. Also it is worth noting that the relationship between u10 and dust AOD is not as high as the one between u10 and dust

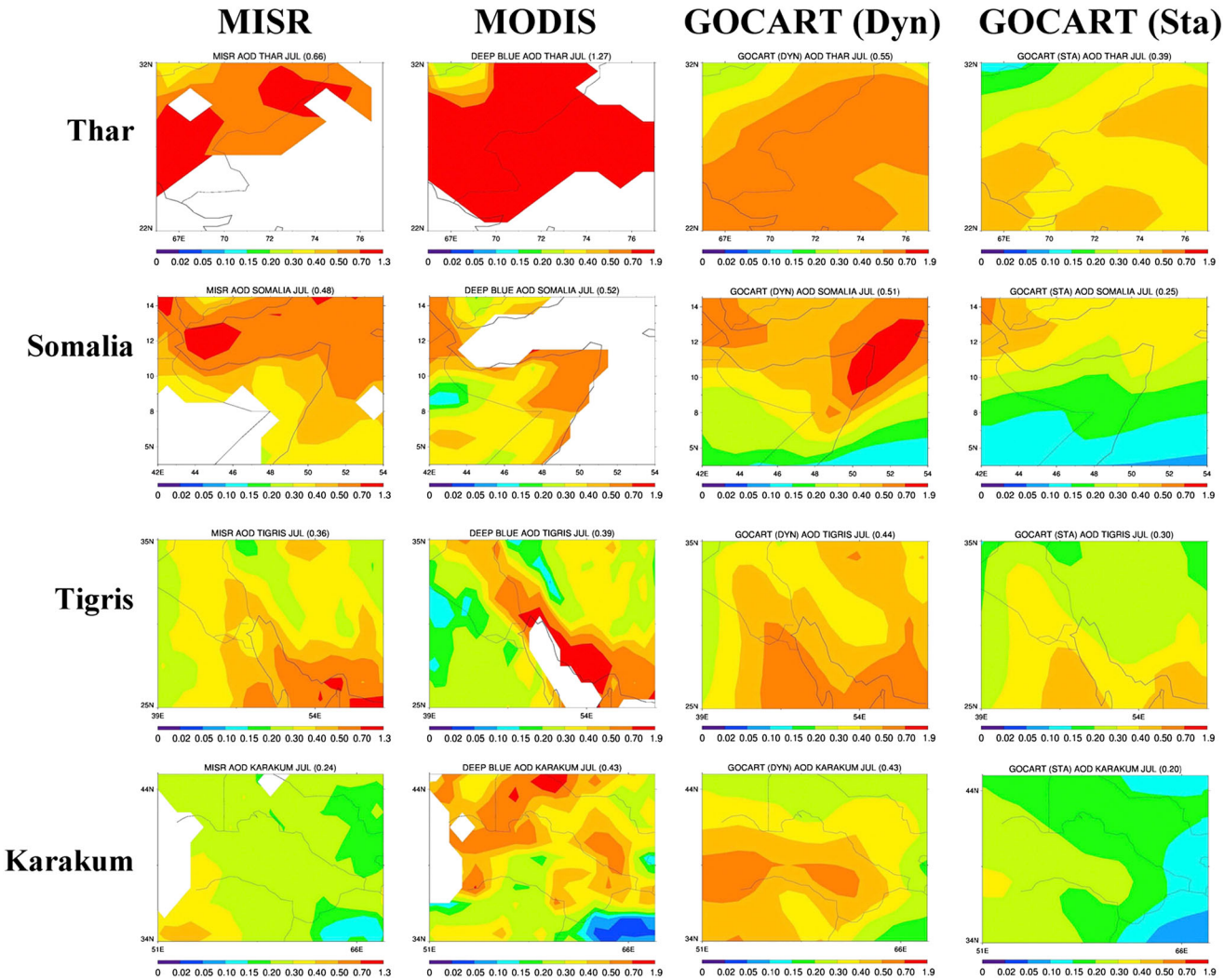

Figure 10. Mean aerosol optical depth map in various source regions in different seasons averaged from 2000 to 2007.

emission, since AOD includes aerosols transported from other source regions.

[26] We also compared the modeled dust AOD with the AERONET database (Figure 12). We selected coarse mode AOD from AERONET since it is mainly from dust. AERONET sites are selected to cover deserts around the world with good quality and temporal coverage (see Figure 4 for the location). Even though the dynamic source function does not show a dramatic improvement in the AERONET comparison, the new dynamic source function show some improvement of the AOD in group II including Australian, Indian, and Sahel region which are shown in the first two columns. Especially at the Tinga Tingana station in Australia, the correlation coefficient is improved from 0.22 to 0.64 and the relative mean bias is improved from 0.81 to 1.04 than the static source function. But the impact of the dynamic source function to other desert stations (third and fourth columns) is negligibly small or negative.

[27] The global distributions of the absolute and relative errors of the two simulations are plotted in January and July (Figures 13a and b). Dust optical depth (DOD) by dynamic source function is 0.02 larger than the static source function in Arabian, Central Asia, and India in July. In Taklimakan desert, DOD by dynamic source function is about 0.5 lower than the static source function in July. The absolute error between two is less than ± 0.05 in most area for two seasons and their global mean difference is less than 2%. Even though the absolute error of DOD is not large, the relative difference between the two simulations is large in both January and July (Figures 13c and d). There are $\pm 20\%$ differences between two simulations not only in source regions but also their downwind area. The relative difference is more extended and larger in July than January. In summer (i.e., July in the Northern Hemisphere and January in Southern Hemisphere), the dynamic source function is larger than the static source function in most source regions except for Chotts and China.

5. Discussion

[28] In this study we choose a single NDVI threshold value of 0.15 globally to determine if the surface is bare or not. However, currently there are no available best estimates on the spatially varying threshold NDVI. A sensitivity test

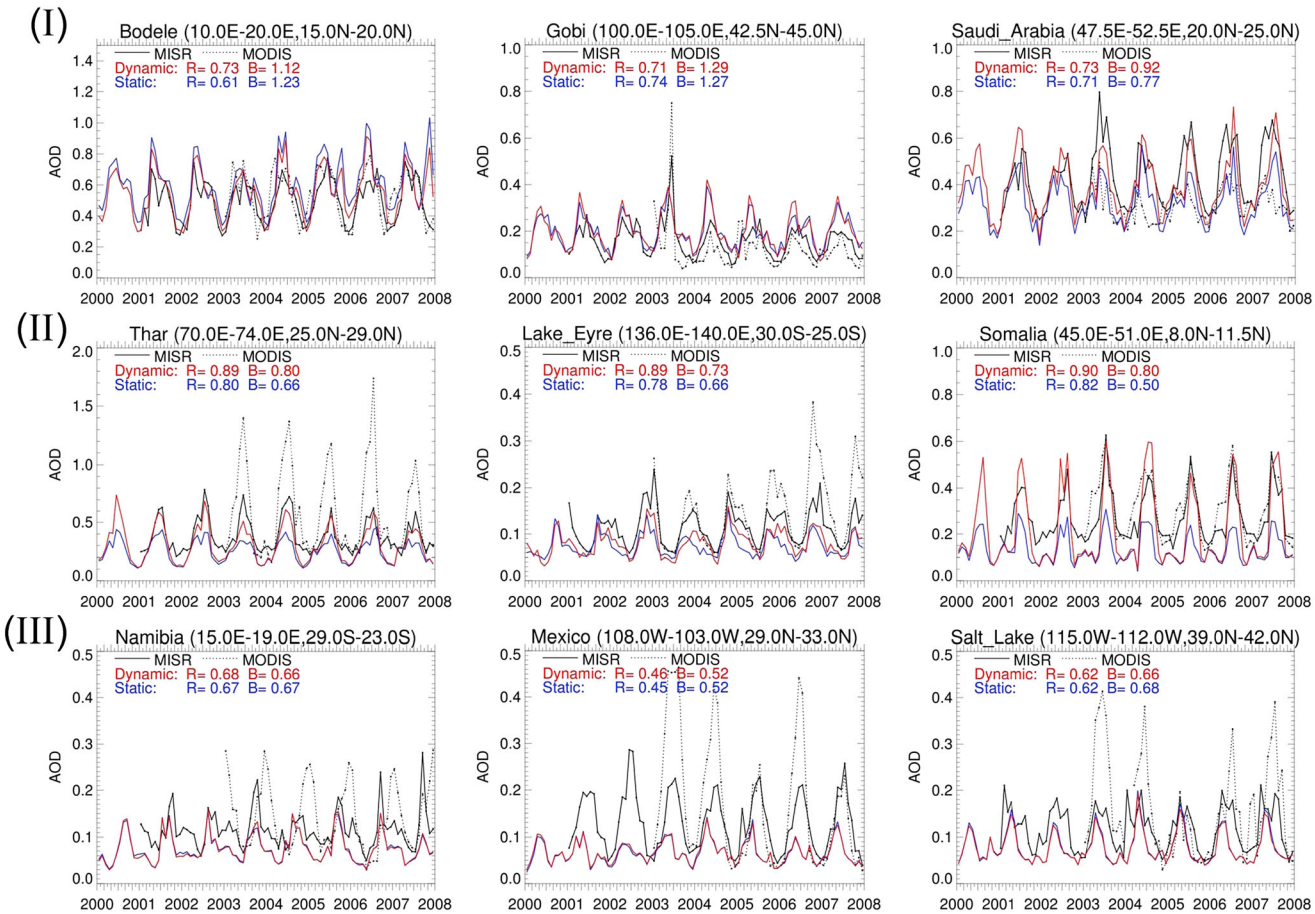

Figure 11. Time series of monthly mean AOD from dynamic (red) and static (blue) source functions, MODIS Deep Blue (black solid line), and MISR (black dotted line). On each panel, R = correlation coefficient, and B = relative mean bias, i.e., $\Sigma(\text{GOCART}i)/\Sigma(\text{AERONET}i)$.

using different threshold NDVI from 0.12 to 0.18 showed a linear relationship between the decrease of threshold NDVI and the increase of percentage bareness (e.g., if threshold NDVI is 0.12, B is increased approximately by 30%). Therefore, further investigation is needed to develop a region-dependent threshold NDVI.

[29] While NDVI identifies bare ground using spectrally dependent light absorption on leaf surface, NDVI itself cannot distinguish the surfaces covered by stem or dead plants from bare ground, therefore it could falsely identify them as bare land in this study. Some previous studies introduced some methods to include the seasonality of land with stem or dead plant [*Tegen et al.*, 2002; *Fairlie et al.*, 2007; *Okin*, 2008], however it remains difficult to quantify their coverage. The inability in detecting soil type, vegetation type by NDVI itself is another limiting factor. These limitation need to be improved in future study.

[30] The present study has shown impacts of the dynamic source function on dust emission even in coarser resolution of $1^\circ \times 1^\circ$. It suggests that developing a dynamic source function with higher spatial resolution can be more beneficial for dust simulation, considering the high heterogeneity of the vegetation within the $1^\circ \times 1^\circ$ area. Such higher spatial resolution dust source function can be constructed with the current 8 km AVHRR NDVI data or with the finer resolution of the MODIS NDVI (e.g., 250 or 500 m resolution), which is available from 2000 to present, and will be easily applicable for finer resolution global- or regional-scale models that are widely used for air quality and aerosol transport studies.

[31] The use of $S_{dynamic}$ and S_{static} in model simulated dust AOD shows noticeable differences in and near source regions especially in the group II, where simulated AOD using $S_{dynamic}$ is up to a factor of two higher than that using S_{static} with significantly improved statistics. On the other hand, global mean dust AOD values from dynamic and static source function are rather similar. This is mainly due to the fact that most dust is emitted in the group I source regions including Sahara desert, which are mostly permanent deserts with NDVI almost always below the threshold value, such that the $S_{dynamic}$ and S_{static} are very similar over those dust source regions (Figure 3). Although the differences between using $S_{dynamic}$ and S_{static} over group I and group III desert areas seem very small for the time period studied in this work, the NDVI-based $S_{dynamic}$ is able to take into consideration of the change of dust source location and area due to the changes of land use and land cover. We have estimated that 88% of dust emission is from the bare land and 12% from vegetated area (e.g., grassland and agriculture land), implying an application of using the NDVI-based approach to develop future dust source scenarios based on

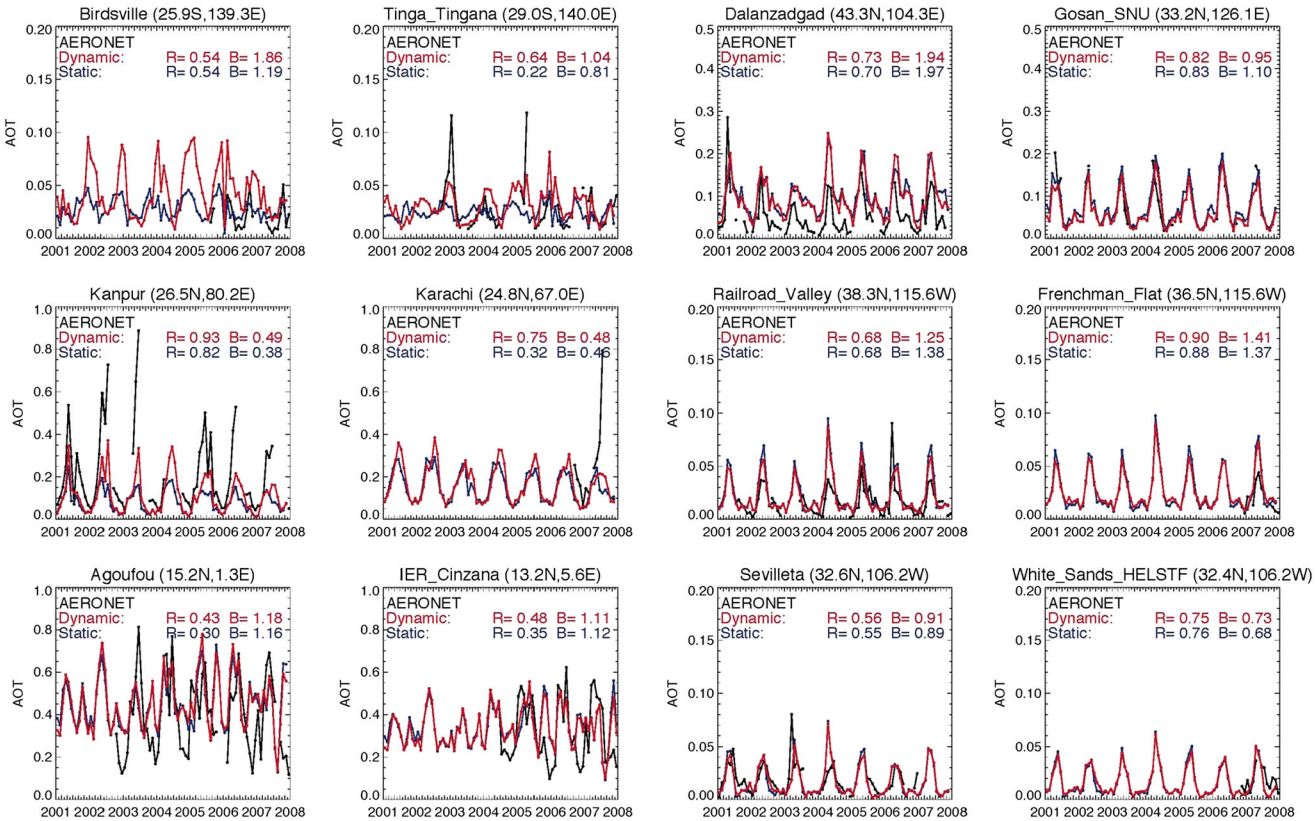

Figure 12. Time series of monthly mean AOD with dynamic (red) and static (blue) source functions compared with AERONET (black). On each panel, R = correlation coefficient, and B = relative mean bias, i.e., $\Sigma(\text{GOCART}i)/\Sigma(\text{AERONET}i)$.

the projections of future land cover and land use change deduced from the change of climate and human activity scenarios.

6. Summary

[32] We have developed a global dynamic source function for estimating dust emissions using a time-resolved surface bareness derived from the AVHRR NDVI. The 15 day surface bareness from 1981 to 2007 at $1^\circ \times 1^\circ$ resolution is calculated as the ratio of the number of 8 km NDVI that is below 0.15 to the total number of 8 km NDVI pixels with the $1^\circ \times 1^\circ$ grid cell. The new dynamic surface bareness, together with the surface topographic depression feature and other surface characteristics (i.e., land cover type, soil depth, soil temperature, snow cover) are used to produce a time-dependent dust source functions to calculate dust emissions in the GOCART model.

[33] We have analyzed the factors that determine the seasonal variation and magnitude of $S_{dynamic}$ over 22 dust source regions over the globe. We have found that these regions can be divided into three groups in terms of the characteristics of surface bareness B and the degree of topographic depression H: (I) permanent deserts where NDVI is almost always below 0.15, resulting in little seasonal variations of $S_{dynamic}$ (e.g., Bodélé and Chotts), (II) seasonal deserts where NDVI has large seasonality and H is high, resulting significant seasonal variations of $S_{dynamic}$ (e.g., Thar, Somalia, and Sahel), and (III) deserts with a low degree of topographic depression H where the large seasonal variation of NDVI has little influence on $S_{dynamic}$ (e.g., Mexico and Namibia).

[34] We conducted two simulations with $S_{dynamic}$ and S_{static}, respectively, from 2000 to 2007 with the GOCART model to test the impact of the $S_{dynamic}$ on dust emission and distribution in the model. The model results have indicated that the dust emission calculated with $S_{dynamic}$ can be a factor of two different from that calculated with S_{static} in some seasons over the group II dust source regions, such as Thar desert, Lake Eyre, Somalia, and Karakum deserts, while it has smaller effects on group I and III deserts. Evaluation of modeled AOD with remote sensing data from MISR, MODIS Deep Blue, and AERONET has shown significantly higher correlation coefficients and lower biases of model calculated AOD with $S_{dynamic}$ compared to that with S_{static} over group II regions and, to some less extent, over group I regions, while no improvements over group III regions. On the global average scale, the AOD from $S_{dynamic}$ and S_{static} are very similar.

[35] With the dust emission calculated from $S_{dynamic}$, we have estimated that globally 88% of dust is emitted from the bare land. Although the vegetated land, such as grassland and crop area, is a minor source of dust emission (12%), they are most susceptible to the change of human activities and climate. Therefore, using the NDVI-based technique may develop a projection of future dust emission from the land cover and land use change scenarios.

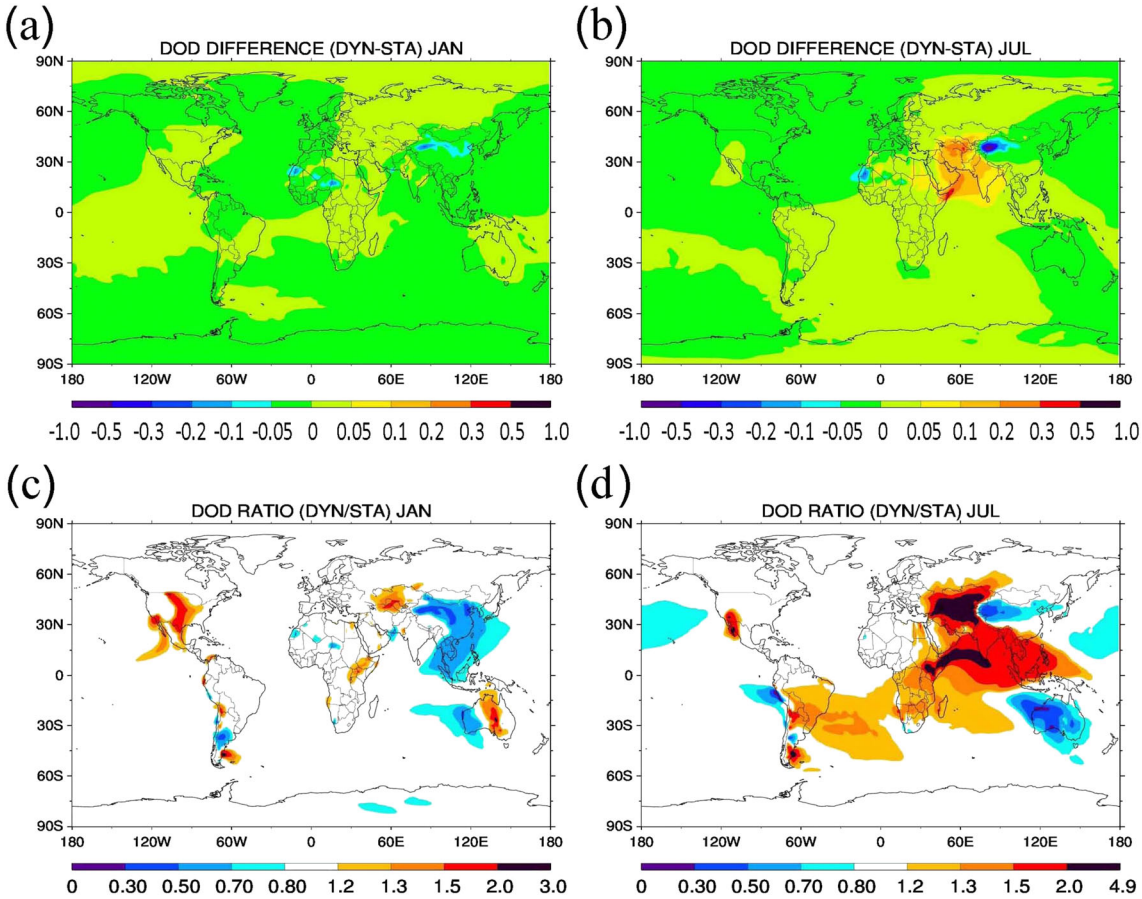

Figure 13. (a and b) Absolute and (c and d) relative differences of dust optical depth (DOD) between dynamic and static source functions in January and July.

[36] **Acknowledgments.** This work is supported by the NASA Modeling, Analysis and Prediction (MAP) and EOS programs. We would like to thank the MISR, MODIS, MODIS Deep Blue, AVHRR, and AERONET teams for the data used in this study.

References

Balkanski, Y. J., D. J. Jacob, G. M. Gardner, W. C. Graustein, and K. K. Turekian (1993), Transport and residence times of tropospheric aerosols inferred from a global three-dimensional simulation of 210 Ph, *J. Geophys. Res.*, *98*, 20,573–20,586.

Bloom, S., *et al*. (2005), Technical report series on global modeling and data assimilation, documentation and validation of the Goddard Earth Observing System (GEOS) Data Assimilation System–Version 4, technical report series on global modeling and data assimilation, *NASA Tech. Memo.*, *TM-2005-104606*, vol. 26. [Available at http://gmao.gsfc.nasa.gov/systems/geos4/Bloom.pdf.]

Bradley, B. A., and J. F. Mustard (2005), Identifying land cover variability distinct from land cover change: Cheatgrass in the Great Basin, *Remote Sens. Environ.*, *94*, 204–213.

Brown, M. E., J. E. Pinzon, K. Didan, J. T. Morisette, and C. J. Tucker (2006), Evaluation of the consistency of long-term NDVI time series derived from AVHRR, SPOT-Vegetation, SeaWIFS, MODIS and Land-SAT ETM+, *IEEE Trans. Geosci. Remote Sens.*, *44*, 1787–1793.

Chin, M., *et al*. (2002), Tropospheric aerosol optical thickness from the GOCART model and comparisons with satellite and Sun photometer measurements, *J. Atmos. Sci.*, *59*(3), 461–483.

Chin, M., T. Diehl, O. Dubovik, T. F. Eck, B. N. Holben, A. Sinyuk, and D. G. Streets (2009), Light absorption by pollution, dust and biomass burning aerosols: A global model study and evaluation with AERONET data, *Ann. Geophys.*, *27*, 3439–3464.

DeFries, R. S., and J. R. G. Townshend (1994), NDVI-derived land cover classification at a global scale, *Int. J. Remote Sens.*, *15*, 3567–3586.

Fairlie, T. D., D. J. Jacob, and R. J. Park (2007), The impact of transpacific transport of mineral dust in the United States, *Atmos. Environ.*, *41*, 1251–1266.

Forster, P., *et al*. (2007), Changes in atmospheric constituents and in radiative forcing, in *Climate Change 2007: The Physical Science Basis, Contribution of Working Group I to the Fourth Assessment Report of the Intergovernmental Panel on Climate Change*, edited by S. Solomon et al., pp. 129–234, Cambridge Univ. Press, Cambridge, U. K.

Fuchs, N. A. (1964), The Mechanics of Aerosols, 408 pp., Pergamon, New York.

Ginoux, P., *et al*. (2001), Sources and distributions of dust aerosols simulated with the GOCART model, *J. Geophys. Res.*, *106*(D17), 20,255–20,273.

Ginoux, P., J. Prospero, O. Torres, and M. Chin (2004), Long-term simulation of dust distribution with the GOCART model: Correlation with the North Atlantic Oscillation, *Environ. Model. Software*, *19*, 113–128.

Ginoux, P., D. Garbuzov, and N. C. Hsu (2010), Identification of anthropogenic and natural dust sources using Moderate Resolution Imaging Spectroradiometer (MODIS) Deep Blue level 2 data, *J. Geophys. Res.*, *115*, D05204, doi:10.1029/2009JD012398.

Giorgi, F., and W. L. Chameides (1986), Rainout lifetimes of highly soluble aerosols and gases as inferred from simulations with a general circulation model, *J. Geophys. Res.*, *91*, 14,367–14,376.

Hansen, M., R. DeFries, J. R. G. Townshend, and R. Sohlberg (2000), Global land cover classification at 1 km resolution using a decision tree classifier, *Int. J. Remote Sens.*, *21*, 1331–1365.

Haywood, J. M., R. P. Allan, I. Culverwell, A. Slingo, S. Milton, J. Edwards, and N. Clerbaux (2005), Can desert dust explain the outgoing longwave radiation anomaly over the Sahara during July 2003?, *J. Geophys. Res.*, *110*, D05105, doi:10.1029/2004JD005232.

Hess, M., P. Koepke, and I. Schult (1998), Optical properties of aerosols and clouds: The software package OPAC, *Bull. Am. Meteorol. Soc.*, *79*, 831–844.

Holben, B. N., *et al*. (1998), AERONET—A federated instrument network and data archive for aerosol characterization, *Remote Sens. Environ.*, *66*, 1–16.

Huneeus, N., *et al*. (2011), Global dust model intercomparison in AeroCom phase I, *Atmos. Chem. Phys.*, *11*, 7781–7816, doi:10.5194/acp-11-7781-2011.

Hsu, N. C., S.-C. Tsay, M. King, and J. R. Herman (2004), Aerosol properties over bright-reflecting source regions, *IEEE Trans. Geosci. Remote Sens.*, *42*, 557–569.

Hsu, N. C., *et al*. (2006), Deep Blue retrievals of Asian aerosol properties during ACE-Asia, *IEEE Trans. Geosci. Remote Sens.*, *44*, 3180–3195.

Husar, R. B., *et al*. (2001), Asian dust events of April 1998, *J. Geophys. Res.*, *106*, 18,317–18,330.

Jickells, T. D., *et al*. (2005), Global iron connections between desert dust, ocean biogeochemistry, and climate, *Science*, *308*, 67–71.

Kahn, R., P. Banerjee, D. McDonald, and D. Diner (1998), Sensitivity of multiangle imaging to aerosol optical depth and a pure size distribution and composition over ocean, *J. Geophys. Res.*, *103*, 32,195–32,213, doi:10.1029/98JD01752.

Kahn, R., P. Banerjee, and D. McDonald (2001), The sensitivity of multiangle imaging to natural mixtures of aerosols over ocean, *J. Geophys. Res.*, *106*, 18,219–18,238, doi:10.1029/2000JD900497.

Kahn, R. A., B. Gaitley, J. Martonchik, D. Diner, K. Crean, and B. Holben (2005), MISR global aerosol optical depth validation based on 2 years of coincident Aerosol Robotic Network (AERONET) observations, *J. Geophys. Res.*, *110*, D10S04, doi:10.1029/2004JD004706.

Koven, C. D., and I. Fung (2008), Identifying global dust source areas using high-resolution land surface form, *J. Geophys. Res.*, *113*, D22204, doi:10.1029/2008JD010195.

Levy, R. C., L. A. Remer, R. G. Kleidman, S. Mattoo, C. Ichoku, R. Kahn, and T. F. Eck (2010), Global evaluation of the Collection 5 MODIS dark-target aerosol products over land, *Atmos. Chem. Phys. Discuss.*, *10*, 14,815–14,873.

Martonchik, J. V., D. J. Diner, R. Kahn, B. Gaitley, and B. N. Holben (2004), Comparison of MISR and AERONET aerosol optical depths over desert sites, *Geophys. Res. Lett.*, *31*, L16102, doi:10.1029/2004GL019807.

Okin, G. S. (2008), A new model of wind erosion in the presence of vegetation, *J. Geophys. Res.*, *113*, F02S10, doi:10.1029/2007JF000758.

Park, S.-U., A. Choe, E.-H. Lee, M.-S. Park, and X. Song (2010), The Asian Dust Aerosol Model 2 (ADAM 2) with the use of normalized difference vegetation index (NDVI) obtained from the Spot4/Vegetation data, *Theor. Appl. Climatol.*, *101*, 191–208.

Peters, A. J., and M. D. Eve (1995), Satellite monitoring of desert plant community response to moisture availability, *Environ. Monit. Assess.*, *37*, 273–287.

Pinzon, J., M. E. Brown, and C. J. Tucker (2005), Satellite time series correction of orbital drift artifacts using empirical mode decomposition, in Hilbert-Huang Transform: Introduction and Applications, edited by N. Huang, pp. 167–186, Global Land Cover Facility, University of Maryland, College Park, Maryland.

Prospero, J. M., P. Ginoux, O. Torres, S. E. Nicholson, and T. E. Gill (2002), Environmental characterization of global sources of atmospheric soil dust identified with the NIMBUS 7 Total Ozone Mapping Spectrometer (TOMS) absorbing aerosol product, *Rev. Geophys.*, *40*(1), 1002, doi:10.1029/2000RG000095.

Remer, L. A., *et al*. (2005), The MODIS aerosol algorithm, products, and validation, *J. Atmos. Sci.*, *62*, 947–973, doi:10.1175/JAS3385. 1.

Shannon, S., and D. J. Lunt (2011), A new dust cycle model with dynamic vegetation: LPJ-dust version 1. 0, *Geosci. Model Dev.*, *4*, 85–105, doi:10.5194/gmd-4-85-2011.

Sobrino, J. A., and N. Raissouni (2000), Toward remote sensing methods for land cover dynamic monitoring: Application to Morocco, *Int. J. Remote Sens.*, *21*, 353–366.

Tegen, I., and I. Fung (1995), Contribution to the atmospheric mineral aerosol load from land surface modification, *J. Geophys. Res.*, *100*, 18,707–18,726, doi:10.1029/95JD02051.

Tegen, I., S. P. Harrison, K. Kohfeld, I. C. Prentice, M. Coe, and M. Heimann (2002), Impact of vegetation and preferential source areas on global dust aerosol: Results from a model study, *J. Geophys. Res.*, *107*(D21), 4576, doi:10.1029/2001JD000963.

Textor, C., *et al*. (2006), Analysis and quantification of the diversities of aerosol life cycles within AeroCom, *Atmos. Chem. Phys.*, *6*, 1777–1813.

Tucker, C. J. (1979), Red and photographic infrared linear combinations for monitoring vegetation, *Remote Sens. Environ.*, *8*, 127–150.

Tucker, C. J., H. E. Dregne, and W. W. Newcomb (1991), Expansion and contraction of the Sahara Desert from 1980 to 1990, *Science*, *253*, 299–301.

Tucker, C. J., J. E. Pinzon, M. E. Brown, D. Slayback, E. W. Pak, R. Mahoney, E. Vermote, and N. El Saleous (2005), An extended AVHRR 8-km NDVI data set compatible with MODIS and SPOT vegetation NDVI data, *Int. J. Remote Sens.*, *26*, 4485–4498.

Webb, N. P. and H. A. McGowan (2009), Approaches to modelling land erodibility by wind, *Prog. Phys. Geogr.*, *33*, 587–613.

Wesely, M. L. (1989), Parameterization of surface resistance to gaseous dry deposition in regional-scale numerical models, *Atmos. Environ.*, *23*, 1293–1304.

Zender, C. S., and E. Y. Kwon (2005), Regional contrasts in dust emission responses to climate, *J. Geophys. Res.*, *110*, D13201, doi:10.1029/2004JD005501.

Zender, C. S., H. Bian, and D. Newman (2003), Mineral Dust Entrainment and Deposition (DEAD) model: Description and 1990s dust climatology, *J. Geophys. Res.*, *108*(D14), 4416, doi:10.1029/2002JD002775.